

Enhanced photovoltaic energy conversion using thermally based spectral shaping

David M. Bierman¹, Andrej Lenert^{1,2}, Walker R. Chan^{3,4}, Bikram Bhatia¹, Ivan Celanović⁴, Marin Soljačić^{3,4} and Evelyn N. Wang^{1*}

Solar thermophotovoltaic devices have the potential to enhance the performance of solar energy harvesting by converting broadband sunlight to narrow-band thermal radiation tuned for a photovoltaic cell. A direct comparison of the operation of a photovoltaic with and without a spectral converter is the most critical indicator of the promise of this technology. Here, we demonstrate enhanced device performance through the suppression of 80% of unconvertible photons by pairing a one-dimensional photonic crystal selective emitter with a tandem plasma-interference optical filter. We measured a solar-to-electrical conversion rate of 6.8%, exceeding the performance of the photovoltaic cell alone. The device operates more efficiently while reducing the heat generation rates in the photovoltaic cell by a factor of two at matching output power densities. We determined the theoretical limits, and discuss the implications of surpassing the Shockley-Queisser limit. Improving the performance of an unaltered photovoltaic cell provides an important framework for the design of high-efficiency solar energy converters.

As a photovoltaic device (PV) can generate electrical power only when illuminated by photons with higher energy than the electronic bandgap of the material ($E_{\text{photon}} > E_g$), the broad spectral nature of sunlight gives rise to the well-known Shockley-Queisser efficiency limit¹. One method of getting beyond this limit is to alter the incident photon spectrum by means of a spectral converter. Luminescence is a common strategy to achieve this photon conversion^{2,3} and demonstrations have successfully taken advantage of energy transitions within various materials^{4–7}. Entrancements in efficiency at the device level have not yet been reported⁸, however, owing to the substantial challenges associated with parasitic self-absorption⁹, strong reflections induced at the spectral converter/vacuum interface⁷, and fabrication of an integrated quantum converter within a solar cell architecture².

To bypass these challenges and enable greater functionality, we have been investigating solar thermophotovoltaic converters (STPVs, Fig. 1a). In this approach, the absorption of sunlight and subsequent re-emission of electromagnetic radiation is achieved through tuned thermal emission from nanophotonic structures. The entire incident photon spectrum is harnessed through a broadband, index-matched thermalization process by a high-temperature ($>1,000^\circ\text{C}$) absorber. This induces thermal excitations within the emitter structure, creating a thermal emission spectrum that generates free electrons that are localized to the conduction band edge in the PV (Fig. 1b). When coupled with strong suppression of sub-bandgap photon emission, high efficiency is attained by means of the spectral shift, while absorbed photon thermalization in the PV cell is reduced and excessive heat generation rates can be eliminated. This effect could enable passive cooling of the PV despite the device typically being under high solar concentration (>100 suns). Additionally, as a thermal engine, STPVs allow for the integration of auxiliary heating¹⁰ and thermal energy storage¹¹ for continuous

operation, the most appealing feature of STPVs relative to other spectral converters. Thus, STPVs have been a particularly attractive technology because they address the common power generation concerns of efficiency, waste heat management, and dispatchability.

Recently, a variety of photonic designs exhibiting spectral control of either reflection¹² or high-temperature thermal emission^{13–16} have been proposed, fabricated and integrated into STPVs^{17–20} for proof-of-concept demonstrations. Shimizu *et al.*^{20,21} created a multi-layer coating consisting of thin-film tungsten and yttria-stabilized zirconia for both the absorber and emitter surfaces. With this material set, they reported an efficiency of $\sim 8\%$; however, their actual experimental efficiency is estimated to be $\sim 0.5\%$ given their reported view factors. Ungaro *et al.*¹⁷ developed a relatively simple fabrication technique to create microtextured absorber/emitter components. They estimated an efficiency of 6.2% using PV fill factors from a different operating point than their thermal demonstration. In addition, their device was tested under laser illumination, which does not capture the STPV spectral conversion process (that is, the narrowing of a broadband source). Although these results show progress in STPVs, a direct comparison of these devices with their underlying PV is lacking and therefore enhanced performance due to an altered spectrum has not been shown.

Here, we successfully pair a tandem plasma-interference optical filter with a one-dimensional Si/SiO₂ photonic crystal thermal emitter to show spectral enhancement in a STPV device. Our theoretical and experimental results indicate that with the addition of this three-component (absorber-emitter-filter) thermally based spectral converter, the overall device can exceed the efficiency of the underlying PV, with demonstrated STPV device conversion rates of 6.8%. In addition, we show reduced waste heat generation in the PV by a factor of two while maintaining the same output power density. This work is an important step towards

¹Device Research Laboratory, Massachusetts Institute of Technology, Cambridge, Massachusetts 02139, USA. ²Department of Mechanical Engineering, University of Michigan, Ann Arbor, Michigan 48109, USA. ³Research Laboratory of Electronics, Massachusetts Institute of Technology, Cambridge, Massachusetts 02139, USA. ⁴Institute for Soldier Nanotechnology, Massachusetts Institute of Technology, Cambridge, Massachusetts 02139, USA.

*e-mail: enwang@mit.edu

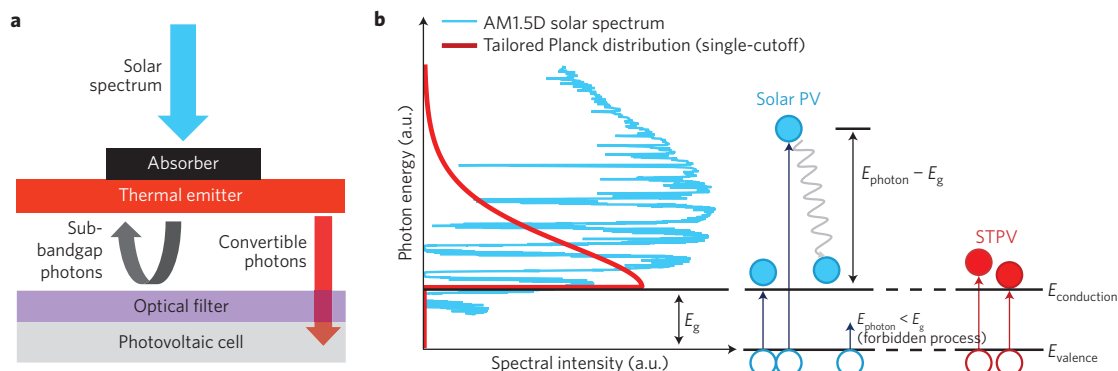


Figure 1 | Operating principle of STPVs and comparison with solar PVs. a, Schematic representation of a solar thermophotovoltaic device. Incident concentrated sunlight is thermalized at the absorber. The generated heat conducts to the thermal emitter surface where, on the basis of the temperature and spectral properties of the surface, engineered thermal emission is directed towards an optical filter. The filter passes photons capable of exciting charge carriers in a single-junction PV cell and reflects back to the emitter those that are not. **b,** Energy conversion mechanisms in the cell comparing illumination by engineered thermal radiation (STPV) with direct solar (PV). The schematic on the right depicts electrons (filled circles) being excited by incident photons from the valence to the conduction band of the semiconductor diode; the intensity of the photon reaching the cell is shown as a function of the photon energy on the left. In the solar PV process, high-energy electrons generate heat within the cell as they decay down to $E_{\text{conduction}}$, where they can be extracted. The STPV process generates an equivalent amount of free electrons but they are localized to $E_{\text{conduction}}$, markedly reducing heat generation in the diode.

realizing a solar-driven power generator capable of producing electricity with a single-junction PV cell at efficiencies exceeding the Shockley–Queisser limit.

Theoretical enhancement due to thermal spectral control

In a STPV device, spectral engineering aims to restrict the thermal radiation reaching the cell to energies above a threshold ($E_{\text{photon}} > E_g$). The desired effective emissivity (achieved by suppressing²² or reflecting²³ low-energy emission modes) is a step function with unity emission relative to the blackbody at energies higher than E_g and no emission of sub-bandgap energy radiation (Fig. 1b). At higher energies, the tail of Planck's distribution naturally limits the flux of photons with excessive energy ($E_{\text{photon}} \gg E_g$). The theoretical limits of this type of single-cutoff-energy STPV conversion deviate from the absolute upper bound previously published²⁴ based on monochromatic photon emission. Therefore, we first determined the limits of this strategy using a few assumptions: the photo-thermal converter is perfectly black and is illuminated by fully concentrated sunlight, the emission spectrum that illuminates the PV cell follows Planck's distribution at supra-bandgap energies and is null for sub-bandgap energies, the PV cell converts the incident light (modified thermal radiation) using the assumptions described in the Shockley–Queisser limit¹—allowing only radiative recombination from a black PV converter, and all non-essential losses are neglected (Supplementary Note 1).

For a single-cutoff strategy, the emitter temperature (T_{emitter}) is a particularly important parameter because it determines the occupation of emission modes above the cutoff energy; as the thermal energy increases relative to the cutoff/bandgap, the supra-bandgap spectral distribution is enhanced and broadened. This is the basis for the fundamental tradeoff between power density and efficiency in STPVs. However, the choice of temperature for a particular bandgap is not trivial. The inset of Fig. 2a shows three representative spectra that illuminate the same PV: $k_B T_{\text{emitter}} = 0.35E_g$ is when the peak of Planck's distribution is aligned with E_g in energy space²⁵, $k_B T_{\text{emitter}} = 0.2E_g$ is when the peak of Planck's distribution is aligned with E_g in wavelength space²⁶, and $k_B T_{\text{emitter}} = 0.1E_g$ is when the Planck's distribution barely overlaps the energy bandgap, where k_B is the Boltzmann constant.

Figure 2a shows the maximum theoretical conversion efficiency as a function of the bandgap for different $k_B T_{\text{emitter}}/E_g$ ratios. A specific, optimum operating temperature for an ideal single-cutoff

STPV exists, which depends on the bandgap of the material. If the thermal energy ($k_B T_{\text{emitter}}$) is high relative to E_g , an excess of high-energy photons illuminate the PV; thermalization of the resulting excited charge carriers reduces the efficiency. At very high temperatures (that is, large bandgaps), re-radiation losses from the absorber are also detrimental to the overall efficiency. On the other hand, smaller temperature differences between the hot (emitter) and cold (PV) reservoirs limit the extracted voltage level (in accordance with the second law of thermodynamics) and thus the ultimate efficiency of the system. The optimum emitter temperature is plotted as a function of PV bandgap energy in Supplementary Fig. 2.

Figure 2a shows how the spectral conversion approach described here can theoretically improve the performance of a solar-to-electrical conversion process over the entire range of the semiconductor materials used as long as the spectral converter temperature is selected appropriately. For the common Si PV cell ($E_g = 1.1$ eV), the maximum achievable efficiency for an ideal single-cutoff emitter STPV converter is 63%, ~40% greater than the Shockley–Queisser limit for this bandgap under fully concentrated sunlight. This efficiency is achieved at a rather high spectral converter temperature of 1,600 °C. For a low-bandgap material, such as the one used experimentally in this work (InGaAsSb, $E_g = 0.55$ eV), the theoretical efficiency limit is ~60% greater than the Shockley–Queisser limit, although the absolute performance is reduced. This efficiency, however, is attained at a more modest and practically achievable optimal temperature of 1,200 °C.

Figure 2b shows the undesired heat generated in each device, comparing solar PV to STPV, normalized by the amount of output electrical power produced. The STPV emitter temperature was optimized at each bandgap. For PV, the heat generation ratio is shown for a blackbody cell and for a cell with perfect reflectance below the bandgap (that is, an ideal back-surface reflector²⁷). We included the latter case because the heat generated from sub-bandgap photons is not intrinsic to the solar PV process. For the low-bandgap cell ($E_g = 0.55$ eV), the heat generated in the cell during the solar PV process is due to thermalization (down to E_g) of nearly the entire solar spectrum. The presence of a thermal spectral converter reduces the normalized heat generation in the cell by a factor of ~3. Reduced heat generation for the same or greater electrical power density relative to sunlight implies spectral enhancement.

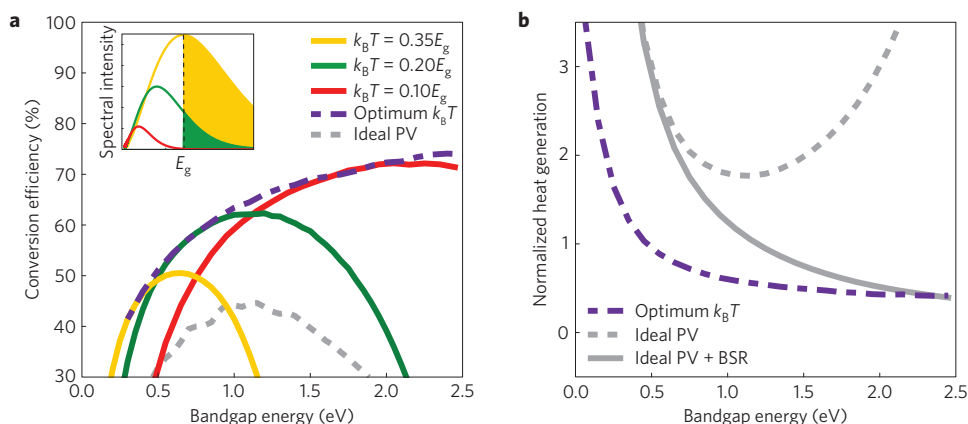


Figure 2 | Theoretical performance of a thermal spectral converter. **a**, Maximum theoretical conversion efficiency as a function of cell bandgap (E_g), comparing the Shockley-Queisser limit for solar PV (dashed) with the single-cutoff STPV with an optimized converter temperature (T) or equivalently, optimized $k_B T/E_g$ ratio (dashed-dotted) and several specific $k_B T/E_g$ ratios. Inset highlights (using a solid fill) the above-bandgap portion of Planck's distribution as a function of increasing $k_B T/E_g$ ratio. The colours correspond to the $k_B T/E_g$ ratios specified in the legend. **b**, Heat generation normalized to the output power density of each device. Solid and dashed curves for the ideal solar PV converter represent with and without an ideal back-surface reflector (BSR), respectively.

However, real devices operate far from these limits because of losses such as: non-radiative recombination and imperfect electrical transport in the cell; and specifically for STPVs, heat losses associated with parasitic thermal radiation from the spectral converter, which take potentially convertible energy away from the PV cell. For a net benefit, the losses associated with spectral conversion must not exceed the additional useful flux delivered to the cell. The ratio of the two curves (PV to STPV) in Fig. 2a indicates the lowest performance of a practical spectral converter compared with an ideal converter (no losses) that must be achieved for an STPV to outperform a solar PV (Supplementary Fig. 1). In the following section, we experimentally show the results of this spectral conversion process using engineered nanophotonic materials.

Nanophotonic converter design and integration

High photo-thermal efficiencies and precise spectral control are required to achieve properties similar to the ideal single-cutoff STPV system, such as the ones shown in Fig. 3a. We used an InGaAsSb PV cell¹² ($E_g = 0.55$ eV) for our demonstration because the necessary operating temperature and spectral properties are not as stringent to achieve spectral enhancement at this bandgap. Incident sunlight is almost entirely absorbed within a multiwalled carbon nanotube (MWCNT) forest^{28–30}. In principle, the introduction of spectral selectivity can further enhance the performance of a STPV, provided that reducing the emittance in the thermal wavelengths does not significantly reduce the absorption of incident sunlight. High solar absorptance is critical when the converter is subject to high optical concentration³¹, as in our experiments. We fabricated a one-dimensional photonic crystal comprised of several Si/SiO₂ layers as the selective thermal emitter¹⁰. Both constructive and destructive wave interference provides a steep cutoff in the spectral emittance at the bandgap of the InGaAsSb PV cell¹². However, >50% of the emitted power cannot be converted at the operating temperature ($\sim 1,000^\circ\text{C}$) owing to the high intrinsic emission of the underlying Si at lower energies (<0.25 eV). As this emission is a direct loss in the system³¹, we incorporated a tandem plasma-interference rugate filter in this study. The filter was engineered to reflect low-energy photons ($E_{\text{photon}} < E_g$) while transmitting the convertible photons ($E_{\text{photon}} > E_g$)^{23,32}.

Optical measurements of the participating surfaces in the spectral converter were used to simulate the resulting illumination spectrum on the cell at a few different emitter temperatures, shown in Fig. 3b. Of the radiation arriving at the 0.55 eV cell, only

$\sim 20\%$ of the energy is carried by photons below its bandgap at an emitter temperature of $1,000^\circ\text{C}$. Qualitatively, we see the entire solar spectrum has been converted much closer to E_g (0.55 eV). Note, however, the conversion is not purely downward because 5% of the AM1.5D spectrum is below the bandgap of the cell. These photons are unable to generate electron-hole pairs if they were to directly illuminate the cell in a solar PV process. In this device, they are thermalized in the absorber and their energy may contribute to the emission of a convertible photon. This is a feature of STPVs that is distinct from other purely downshifting strategies.

Characterization of spectral converter

We performed a series of experiments to observe the effects of the spectral converter on the performance of the solar conversion process. We directly compared the operation of a cell with and without the presence of our spectral converter. To quantify the conversion performance of the device, we define efficiency as the ratio of electrical power generated by the device to the radiative power incident on the absorber surface

$$\eta_{\text{device}} = \frac{\text{MPP}_{\text{PV}}}{\dot{Q}_{\text{solar}}} = \frac{\dot{W}_{\text{elec}}'' A_{\text{PV}}}{\dot{Q}_{\text{solar}}} \quad (1)$$

where MPP_{PV} is the maximum power operating point of the PV cell, \dot{Q}_{solar} is the radiative power that impinges each absorber surface, \dot{W}_{elec}'' is the measured electrical power density, and A_{PV} is the total PV area in the device.

We first characterized the InGaAsSb¹² cell by exposing it to a simulated AM1.5D solar spectrum over a wide range of input fluxes (50–100 suns). As expected, the generated photocurrent density scaled linearly with solar illumination in this range. The increasing photocurrent was accompanied by a logarithmic increase in open-circuit voltage and a slight decrease in fill factor due to the presence of parasitic series resistance. This led to a relatively constant conversion efficiency that will be discussed later.

For comparison, we shielded the InGaAsSb PV from the solar spectrum with the spectral converter and repeated the experiment. We designed our spectral converter to be 4 cm^2 to markedly improve the thermal performance from our previous work (1 cm^2 ; ref. 18). This scale-up decreased the amount of side losses relative to the primary radiation flows. Owing to the limited availability of the InGaAsSb cells, we used the same converter (1 cm^2) as the first experiment. Thus, inactive PV cells were arranged below the filter to

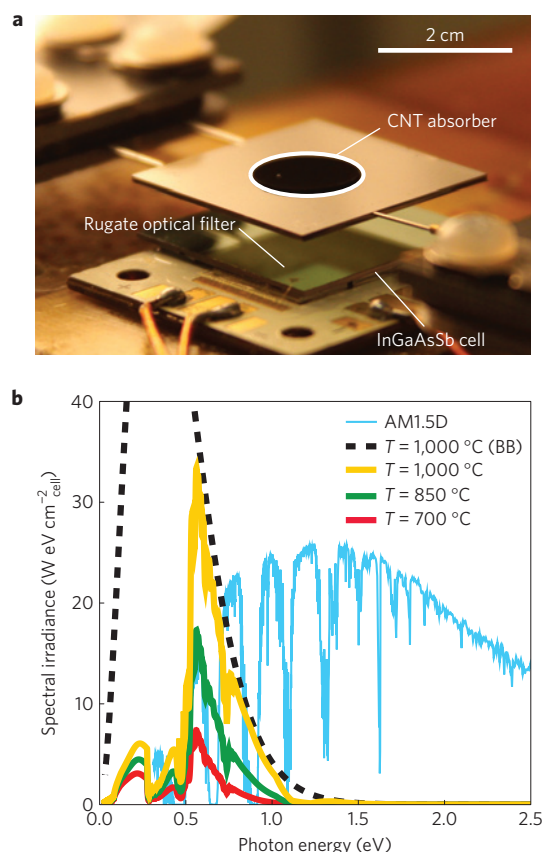


Figure 3 | Spectrally engineered STPV device. **a**, Optical image of the solar thermophotovoltaic device constructed in this study to observe the spectral enhancement process. The backside of the suspended converter (not shown) is the Si/SiO₂ selective emitter. **b**, Simulated spectral irradiances reaching the PV cell for a few different temperatures. Modification of the blackbody spectrum (BB) comes both from the spectrally selective Si/SiO₂ emitter as well as the rugate optical filter. Also shown is the AM1.5D solar spectrum at an optical concentration of 100 suns (which is typical for STPVs with matching emitter and absorber areas¹⁸).

match the emitter area (3 cm² of inactive cells + 1 cm² of active cells, Supplementary Fig. 3a). Owing to the high reflectivity of the rugate filter at sub-bandgap energies (Supplementary Fig. 3b), the effect of the inactive PV cell area on the energy balance was negligible.

Given the geometry of the spectral converter, thermal gradients due to the spreading of absorbed power in the CNT forest, and local view factor variations are expected. To address this, we took advantage of the symmetry of the device—the net radiation exchange in any one of the four quadrants on the emitter surface is spatially equivalent. Thus, the average photocurrent density generated in the active PV cell is representative of the entire emitter area. For the STPV experiments, the MPP_{PV} was determined by finding the $MPP_{active\ PV}$ and scaling it to meet the total PV area, validated by the experiments described in the Supplementary Fig. 3b.

As in the solar PV experiment, we varied the incident radiation on the absorber and recorded the electrical characteristics of our active PV cell. Two different STPV devices were tested. One of them (STPV 1) had a smaller absorber relative to the emitter surface area ($A_{emitter}/A_{absorber} = 12$) and the other (STPV 2) had a larger absorber ($A_{emitter}/A_{absorber} = 7$). The smaller absorber demonstrated reduced thermal re-emission losses and therefore more efficient device operation. The input power to all devices (solar PV and STPV) was provided by a solar simulator; in some STPV cases, this light source was supplemented by a xenon-arc broadband source to

achieve higher emitter temperatures (see Methods). More about the optical configuration is provided in Supplementary Fig. 5.

Figure 4a shows that in contrast to the conversion efficiency of the solar PV process, which remained relatively constant with increasing output electrical power, the measured STPV efficiency reached $6.8 \pm 0.2\%$, which is higher than previously reported values of comparable measurements. This result is attributed to the vastly improved spectral control and increased scale. Our experimental results (shown as circles) show good agreement with our isothermal radiative transfer model shown as smooth lines (see our previous work³³ for more details regarding the model). At low output power densities, the device conversion efficiency of the PV cell was much higher than that of the STPV device because the temperature of the thermal emitter was too low. However, as the emitted photon flux became more energetic at higher temperatures (Fig. 3b), there was a transition to a regime where the spectral conversion strategy exceeded the overall efficiency of the solar-to-electrical conversion of the directly illuminated cell (solar PV).

This experimental demonstration of a STPV device exceeding the performance of a solar PV with the same cell successfully exhibits the enhancement gained from spectral conversion; the losses introduced by the absorption/re-emission process were outweighed by the improvement gains from converting the solar spectrum. Our model³³ indicates that at our highest measured efficiency point, ~68% of incident power was delivered to the cell in the form of a modified spectrum, ~10.2% of which was converted by the cell into electrical power. Our model suggests that increasing the input power further (and therefore $T_{emitter}$) would allow the STPV device to continue to exceed the conversion efficiency of this PV cell and reach overall efficiencies approaching 10% for this particular experiment.

From a heat generation perspective, the two spectra (solar and thermally modified) shown in Fig. 3b produced markedly different heat loads on the cell. As the bandgap of the InGaAsSb cell is energetically almost entirely below the solar spectrum, a large portion of the incident energy contributed to heat generation. When the cell is illuminated by the lower energy spectrum that is produced by the spectral converter, the resulting heat generation is substantially reduced. Figure 4b shows the measured heat generation in the PV cell for the experiments. At 0.35 W cm^{-2} of electrical power density, the solar PV generated $\sim 2\times$ more heat in the cell than the STPV despite having the same conversion efficiency (to within the error of the measurement). Excessive heat loads must be dissipated with higher heat transfer coefficients to prevent an increase in cell temperature and thus reduced electrical performance³⁴.

Discussion

This experimental demonstration of spectral enhancement using a single-cutoff scheme provides deeper insight into the conversion process. The transformation of the solar spectrum into a narrow-band thermal spectrum is, in principle, independent of the quality of the PV cell used in the device. By revisiting the idealized PV cell introduced in the theoretical section that operates at the Shockley–Queisser limit under a given solar illumination, we show in Fig. 5 that incorporating our spectral converter would enhance the conversion rate and thus exceed this limit, despite an un-optimized design and non-ideal spectral components (provided the input beam could be further concentrated for sufficient thermal performance). According to the analysis, the crossover point at which the STPV meets the Shockley–Queisser limit occurs at an emitter temperature of $\sim 1,300^\circ\text{C}$ and an optical concentration of $\sim 2,000\times$ on the STPV absorber (corresponding to $\sim 200\times$ on the idealized PV owing to the introduced area ratio). Furthermore, a scaled-up spectral converter constructed of the same material set that operates at the same temperature with an input power of $>4\text{ kW}$

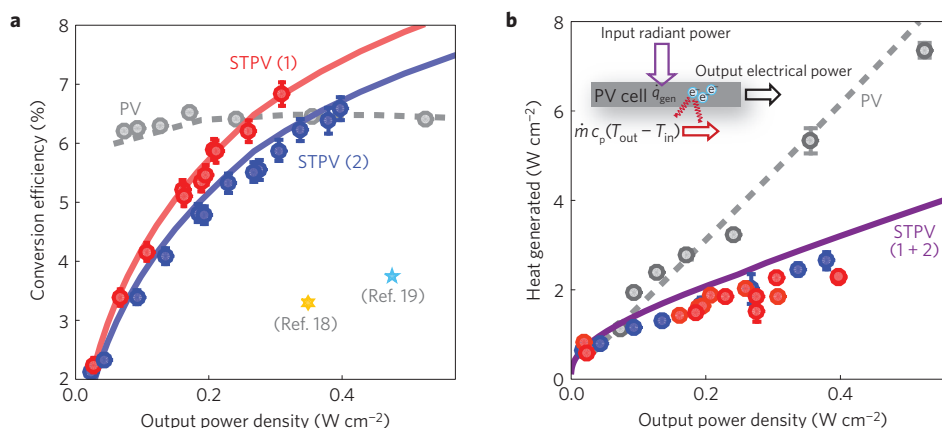


Figure 4 | Experimental results of efficiency and heat generation. **a**, Converter device performances for both STPV and PV with an InGaAsSb ($E_g = 0.55$ eV) cell. The STPV exceeds the PV conversion efficiency for a given output power density at sufficiently high temperatures. STPV (1) has a smaller absorber than STPV (2) and thus operates more efficiently for a particular output power. The dotted lines are generated from a PV model whereas the solid lines come from a STPV model³³. **b**, Heat dissipated by the cooling loop in both the PV and STPV experiments to maintain the PV converter at an equilibrium temperature (Supplementary Fig. 4). Reducing the illumination of the PV cell with unusable photons improves efficiency and markedly reduces heat generation. The inset schematically shows the calorimetric method used to determine heat generation rate, which is the product of the water mass flow rate (\dot{m}), the specific heat capacity (c_p) and the temperature differential between the outlet (T_{out}) and inlet (T_{in}), normalized by the total PV cell assembly area (A_{PV}). The error bars were evaluated on the basis of propagation of the standard deviation (using a t -distribution with a 95% confidence interval), instrument error and resolution error.

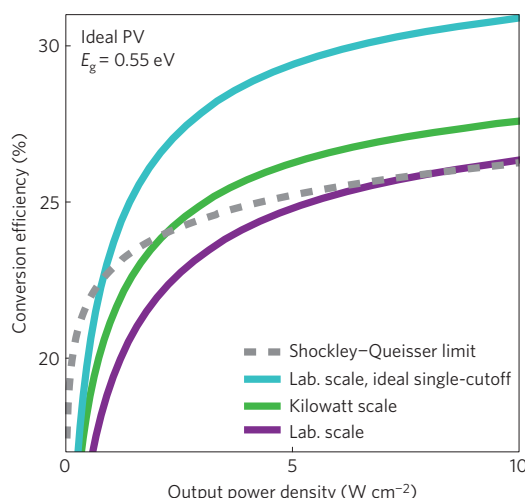


Figure 5 | Nanophotonic material set in the radiative limit. Predicted performances of the three-component spectral converter demonstrated in this work when paired with a PV ($E_g = 0.55$ eV) that operates in the radiative limit; shown as a function of device scale: 4 cm^2 converter as demonstrated in this work, and at a kilowatt scale (400 cm^2). For comparison, the Shockley-Queisser limit (dashed) shows the performance of the same ideal PV under AM1.5D solar illumination. Also shown is the laboratory-scale device with an ideal single-cutoff emitter, as used to calculate the theoretical limits in Fig. 1.

(where parasitic heat losses from the supports and device edges are less than 1% of the input power) would further improve the efficiency of this converter by ~ 10 –15%. The crossover point in this case is at a moderate emitter temperature of $\sim 1,000^\circ\text{C}$ and an optical concentration of $\sim 80\times$ on the STPV absorber ($\sim 80\times$ on the idealized PV). Thus, moving to larger devices plays an important role in exceeding the Shockley-Queisser limit at more feasible operating conditions. Included in the figure is the performance of our device with the ideal single-cutoff emitter used to calculate the theoretical limits, indicating that our demonstrated spectral converter is only $\sim 15\%$ worse than this ideal case.

Any spectral modification strategy implemented between the sun and a PV needs to perform well enough to justify the losses introduced to the system. Although this demonstration was performed on a low-bandgap cell, our theoretical analysis suggests that this thermally based spectral enhancement can be extended to wider-bandgap materials to reach higher efficiencies. As the development of refractory photonic materials continues to grow rapidly, higher-quality emission spectra will be delivered to the PV cell. Future studies should continue to seek high spectral control with cost-effective and scalable components as the field begins to approach commercializable solar energy converters.

Methods

Fabrication and assembly of active components. Fabrication of the active components has been previously reported in the literature: absorber³⁵, emitter¹⁰, optical filter³², cell¹². Specifically, to prepare the absorber-emitter, the procedure described in ref. 18 was adapted for larger samples. The MWCNT absorbers were grown using a chemical vapour deposition process and the Si/SiO₂ layers of the emitter (one-dimensional photonic crystal) were deposited by low-pressure and plasma-enhanced chemical vapour deposition¹⁰. The absorber and emitter were fabricated on either side of a silicon substrate ($550\text{ }\mu\text{m}$ thickness). The tandem plasma-interference optical filter was purchased from Rugate Technologies, and it consists of an interference filter in series with a plasma filter³². The InGaAsSb diode was fabricated at Lincoln Laboratory¹². The filter-cell assembly was constructed by epoxying the cold-side tandem filter directly to the InGaAsSb cell (and to the surrounding dummy cells) using optically transparent³⁶ polydimethylsiloxane (PDMS; see Supplementary Fig. 3). PDMS was chosen for its optical transmittance. The PDMS was applied thinly and uniformly over the active and inactive PV areas and the optical filter was gently pressed down and aligned over the PV area. The epoxy was allowed to cure overnight on a hot plate at 50°C leading to a strong bond that preserved its high transmittance. Although the thermal conductivity of PDMS is relatively low ($\sim 0.15\text{ W mK}^{-1}$; ref. 37), the thickness is assumed to be of the order of the roughness of the material ($<1\text{ }\mu\text{m}$), which suggests a negligible temperature drop between the optical filter and the cell surface.

Construction and alignment of the integrated device. We developed a systematic procedure for repeatable alignment and gap control between the emitter and optical filter, and between the absorber and the aperture/shield (see ref. 18 for more detailed layout information). The PV cell assembly was first mounted to the heat collection device that was fixed to a z -axis stage (122-0101, Opto Sigma). The absorber-emitter was then placed on the optical filter; as the filter and the absorber-emitter have equal dimensions, the sample edges were aligned with the filter edges using a vertical straight edge. The mechanical support needles were

brought into contact with two edges of the absorber–emitter to secure its position while maintaining alignment with the PV cell. Two hypodermic needles (27Gx1.25", B-D) were used on one side of the sample and a spring-loaded pin (POGO-72U-S, ECT) on the opposite side for mechanical support. This design minimized pitch errors due to thermal expansion of the sample during operation. The gap between the emitter and the PV cell was set using the z-stage to lower the PV cell assembly. The experimental set-up was then mounted in the vacuum chamber and aligned with the aperture/shield using a manual linear stage. The chamber was evacuated during STPV experiments (<0.5 Pa). A ~ 300 μm gap separated the emitter from the front surface of the optical filter (thickness of 400 μm) such that the diffuse view factor between the emitter and the PV cell was approximately 96%.

Spectral properties. The spectral properties of the following components have been previously reported in the literature: absorber²⁹, emitter^{10,18}. Further, the spectral properties of the optical filter when bonded to the InGaAsSb cell (as well as a black substrate) are shown in Supplementary Fig. 3b.

Measurement of output power. We performed current–voltage (I – V) sweeps using a source meter (2440, Keithley Instruments) when the PV reached quasi-steady state at the particular operating point being studied. The sweep was conducted in a 4-wire configuration with 50 points acquired in the range of 0–0.7 V. The maximum power point (MPP_{PV}) is the maximum of the product of the current and the voltage.

To verify that the energy balance of the device was not altered by having one quadrant of the PV area active (Supplementary Fig. 3a), we studied the optical properties of the optical filter with various backing materials. These measurements were performed using an FT-IR (FT-IR 6700, Thermo Fisher) with a DTGS detector and a KBr beam splitter. The FT-IR spectrum of the rugate filter bonded to the InGaAsSb cells, Si painted with HE-6, or Ag is shown in Supplementary Fig. 3b. The data indicate that the reflectance remains approximately unchanged when the active cell is swapped out for a highly absorbing substrate. For that reason, the dummy cells, which populate the inactive PV area, were painted with black paint (HE-6, Rolls Royce). In this approach, the absence of active cells is expected to have a negligible impact on the absorber–emitter temperature distribution and the output power from the active quadrant (note: the potential impact of radiative recombination in the cell on the absorber–emitter temperature was neglected because the cell efficiency is relatively low). Further, when the inactive cells are placed in a configuration as shown in Supplementary Fig. 3a, owing to symmetry, the power extracted from the single active quadrant (that is, the active PV area) can be scaled by a factor of four to determine the total STPV electrical power generated.

Cell thermal management and heat load calorimetry. The temperature of the cell in the experiments was monitored by a thermocouple (Type J, Omega Engineering) sandwiched between the PV cell and a copper cooling block (CP25, Lytron). The temperature was recorded at each data point. The difference in cell temperature between the PV and STPV experiments is small (less than 6°) as shown in Supplementary Fig. 4a. We also characterized the cell performance as a function of temperature by fixing the input radiation spectrum and varying the inlet cooling water temperature. Supplementary Fig. 4b indicates that the relative change in performance (that is, maximum power that can be extracted for a given input spectrum) as a function of increasing temperature is highly linear in this regime with a slope of $0.76\% \text{ K}^{-1}$ (R^2 value of 0.995). For a difference in temperature of 6 K, we expect a maximum difference of less than 6% (relative) due to the temperature dependence. (Note: the slightly warmer cell temperature during the STPV experiment is not due to higher heat generation.)

To quantify the heat generation in the cell during the PV and STPV experiments, we monitored the amount of heat dissipation required to keep the cell at a fixed temperature (Supplementary Fig. 4). This was performed using a cooling loop in thermal contact with the PV cell through a thin copper block. The inlet and outlet temperatures of the water that passed through the copper block were measured with two thermocouples (Type J, Omega Engineering). The flow rate was regulated with a peristaltic pump (Masterflex EW-07522-20, Cole-Parmer). The overall heat generated (W cm^{-2}) is the product of the water mass flow rate (kg s^{-1}), the specific heat capacity ($\text{J kg}^{-1} \text{ K}^{-1}$) and the temperature differential between the inlet and outlet (K), normalized by the total PV cell assembly area, A_{PV} (cm^2). It should be noted that in the STPV experiments, the heat generated is normalized by the full area of the optical filter (4 cm^2) because the dummy cells provide a conductive heat path to the cold loop. Both the PV and the STPV heat generation data were acquired without an external electrical load; the reported heat load data were corrected accordingly by subtracting the total electrical output power from the total heat generation without an external electrical load.

Solar-simulating light source. The solar simulator used in the experiment (92192, Newport Oriel) was able to provide a maximum flux of ~ 400 suns. \dot{Q}_{solar}

was measured at the absorber plane using a thermopile detector (919P-040-50, Newport) for each MPP_{PV} data point recorded. The input power was varied by moving the concentrating lens such that the focal plane is translated relative to the absorber plane. To boost the input power (and thus the emitter temperature), we integrated a mercury–xenon arc lamp (66142, Newport) in the set-up shown in Supplementary Fig. 5a. The auxiliary beam is a broadband white light source that, like the primary solar simulator beam, undergoes near perfect thermalization on interaction with our blackbody absorber. Using this source, we were able to boost the max input power by $\sim 25\%$. Supplementary Fig. 5b shows the same data as Fig. 4a, but indicates which of the operating points correspond to which input power. As indicated by the figure, it is the integrated value of input power that drives the temperature of the device owing to the spectral independence of the MWCNT absorber.

Measurement uncertainty. Unless otherwise specified, uncertainty in the reported experimental values was evaluated on the basis of propagation of the following errors: standard deviation (using a t -distribution with a 95% confidence interval), instrument error, and resolution error.

Received 21 October 2015; accepted 21 April 2016;
published 23 May 2016

References

- Shockley, W. & Queisser, H. J. Detailed balance limit of efficiency of p–n junction solar cells. *J. Appl. Phys.* **32**, 510–519 (1961).
- Wegh, R. T. Visible quantum cutting in $\text{LiGdF}_4\text{:Eu}^{3+}$ through downconversion. *Science* **283**, 663–666 (1999).
- Trupke, T., Green, M. A. & Würfel, P. Improving solar cell efficiencies by down-conversion of high-energy photons. *J. Appl. Phys.* **92**, 1668–1674 (2002).
- Shalav, A., Richards, B. S. & Green, M. A. Luminescent layers for enhanced silicon solar cell performance: up-conversion. *Sol. Energy Mater. Sol. Cells* **91**, 829–842 (2007).
- Richards, B. S. Luminescent layers for enhanced silicon solar cell performance: down-conversion. *Sol. Energy Mater. Sol. Cells* **90**, 1189–1207 (2006).
- Manor, A., Martin, L. & Rotschild, C. Conservation of photon rate in endothermic photoluminescence and its transition to thermal emission. *Optica* **2**, 585–588 (2015).
- Wang, H.-Q., Batentschuk, M., Osvet, A., Pinna, L. & Brabec, C. J. Rare-earth ion doped up-conversion materials for photovoltaic applications. *Adv. Mater.* **23**, 2675–2680 (2011).
- Fix, T., Rinnert, H., Blamire, M. G., Slaoui, A. & MacManus-Driscoll, J. L. Nd:SrTiO_3 thin films as photon downshifting layers for photovoltaics. *Sol. Energy Mater. Sol. Cells* **102**, 71–74 (2012).
- Boccolini, A., Marques-Hueso, J., Chen, D., Wang, Y. & Richards, B. S. Physical performance limitations of luminescent down-conversion layers for photovoltaic applications. *Sol. Energy Mater. Sol. Cells* **122**, 8–14 (2014).
- Chan, W. R. *et al.* Toward high-energy-density, high-efficiency, and moderate-temperature chip-scale thermophotovoltaics. *Proc. Natl Acad. Sci. USA* **110**, 5309–5314 (2013).
- Datas, A., Chubb, D. L. & Veeraragavan, A. Steady state analysis of a storage integrated solar thermophotovoltaic (SISTPV) system. *Sol. Energy* **96**, 33–45 (2013).
- Dashiell, M. W. *et al.* Quaternary InGaAsSb thermophotovoltaic diodes. *IEEE Trans. Electron Devices* **53**, 2879–2891 (2006).
- Stelmakh, V. *et al.* *SPIE Sens. Technol. Appl.* (International Society for Optics and Photonics, 2014).
- Rinnerbauer, V. *et al.* High-temperature stability and selective thermal emission of polycrystalline tantalum photonic crystals. *Opt. Express* **21**, 11482–11491 (2013).
- Wang, Z. *et al.* Tunneling-enabled spectrally selective thermal emitter based on flat metallic films. *Appl. Phys. Lett.* **106**, 101104 (2015).
- Li, W. *et al.* Refractory plasmonics with titanium nitride: broadband metamaterial absorber. *Adv. Mater.* **26**, 7921 (2014).
- Ungaro, C., Gray, S. K. & Gupta, M. C. Solar thermophotovoltaic system using nanostructures. *Opt. Express* **23**, A1149 (2015).
- Lenert, A. *et al.* A nanophotonic solar thermophotovoltaic device. *Nature Nanotech.* **9**, 126–130 (2014).
- Rinnerbauer, V. *et al.* Metallic photonic crystal absorber–emitter for efficient spectral control in high-temperature solar thermophotovoltaics. *Adv. Energy Mater.* **4**, 1400334 (2014).
- Shimizu, M., Kohiyama, A. & Yugami, H. High-efficiency solar-thermophotovoltaic system equipped with a monolithic planar selective absorber/emitter. *J. Photon. Energy* **5**, 053099 (2015).
- Shimizu, M., Kohiyama, A. & Yugami, H. *SPIE Photonics Europe* (International Society for Optics and Photonics, 2014).

22. Rinnerbauer, V. *et al.* Large-area fabrication of high aspect ratio tantalum photonic crystals for high-temperature selective emitters. *J. Vac. Sci. Technol. B* **31**, 011802 (2013).
23. Ortabasi, U. Rugate technology for thermophotovoltaic (TPV) applications: a new approach to near perfect filter performance. *AIP Conf. Proc.* Vol. 653, 249–258 (AIP, 2003).
24. Harder, N.-P. & Wurfel, P. Theoretical limits of thermophotovoltaic solar energy conversion. *Semicond. Sci. Technol.* **18**, S151–S157 (2003).
25. Lenert, A. *et al.* Addendum: a nanophotonic solar thermophotovoltaic device. *Nature Nanotech.* **10**, 563 (2015).
26. Chubb, D. *Fundamentals of Thermophotovoltaic Energy Conversion* (Elsevier B. V., 2007).
27. Coutts, T. J. & Ward, J. S. Thermophotovoltaic and photovoltaic conversion at high-flux densities. *IEEE Trans. Electron Devices* **46**, 2145–2153 (1999).
28. Lin, M., Shyu, F. & Chen, R. Optical properties of well-aligned multiwalled carbon nanotube bundles. *Phys. Rev. B* **61**, 14114–14118 (2000).
29. Mizuno, K. *et al.* A black body absorber from vertically aligned single-walled carbon nanotubes. *Proc. Natl Acad. Sci. USA* **106**, 6044–6047 (2009).
30. Yang, Z.-P., Ci, L., Bur, J. A., Lin, S.-Y. & Ajayan, P. M. Experimental observation of an extremely dark material made by a low-density nanotube array. *Nano Lett.* **8**, 446–451 (2008).
31. Lenert, A., Nam, Y., Bierman, D. M. & Wang, E. N. Role of spectral non-idealities in the design of solar thermophotovoltaics. *Opt. Express* **22**, A1604–A1618 (2014).
32. Rahmlow, T. D. *et al.* *AIP Conf. Proc.* **738**, 180–188 (2004).
33. Bierman, D. M., Lenert, A. & Wang, E. N. Investigation of design parameters in planar solar thermophotovoltaic devices. *15th International Heat Transfer Conference (IHTC-15)* (2014).
34. Wysocki, J. J. & Rappaport, P. Effect of temperature on photovoltaic solar energy conversion. *J. Appl. Phys.* **31**, 571–578 (1960).
35. Nessim, G. D. *et al.* Tuning of vertically-aligned carbon nanotube diameter and areal density through catalyst pre-treatment. *Nano Lett.* **8**, 3587–3593 (2008).
36. Fujii, T. PDMS-based microfluidic devices for biomedical applications. *Microelectron. Eng.* **61–62**, 907–914 (2002).
37. Mark, J. *Polymer Data Handbook* (Oxford Univ. Press, 1999).

Acknowledgements

This work was supported as part of the Solid-State Solar Thermal Energy Conversion (S³TEC) Center, an Energy Frontier Research Center funded by the US Department of Energy, Office of Science, Basic Energy Sciences under Award no. DE-FG02-09ER46577. The authors thank C. Wang from Lincoln Laboratory for providing the InGaAsSb cells; H. Mutha, D. Li and C.V. Thompson's group (for help with CNT growth); W. Lee and IDAX Microelectronics Labs, Inc. (PV cell packaging); K. Broderick and Microsystems Technology Laboratories (spectral converter/aperture fabrication); K. Bagnall and J. Tong (optical configuration advice); the Device Research Lab (for critique); M. N. Luckyanova, G. Chen and the Nanoengineering group (for advice and experimental aid).

Author contributions

All authors contributed extensively to this work. D.M.B. and A.L. designed the experimental and theoretical studies, constructed the experimental model, and wrote the paper. D.M.B. and B.B. designed and fabricated components for the device scale-up. D.M.B. wrote the code for the theoretical study and executed the experiments. W.R.C. designed and fabricated the emitter. I.C., M.S. and E.N.W. supervised and guided the project.

Additional information

Supplementary information is available [online](https://www.nature.com/online). Reprints and permissions information is available online at www.nature.com/reprints. Correspondence and requests for materials should be addressed to E.N.W.

Competing interests

The authors declare no competing financial interests.